

Fast Near-Infrared Photodetection using III-V Colloidal Quantum Dots

Bin Sun, Amin Morteza Najarian, Laxmi Kishore Sagar, Margherita Biondi, Min-Jae Choi, Xiyan Li, Larissa Levina, Se-Woong Baek, Chao Zheng, Seungjin Lee, Ahmad R. Kirmani, Randy Sabatini, Jehad Abed, Mengxia Liu, Maral Vafaie, Peicheng Li, Lee J. Richter, Oleksandr Voznyy, Mahshid Chekini⁴, Zheng Hong Lu, F. Pelayo García de Arquer and Edward H. Sargent**

B. Sun^[+], A. Morteza Najarian, L. Kishore Sagar, M. Biondi, M.-J. Choi, X. Li, L. Levina, S.-W. Baek, C. Zheng, S. Lee, R. Sabatini, J. Abed, M. Liu, M. Vafaie, O. Voznyy, F. P. García de Arquer** and E. H. Sargent**

Department of Electrical and Computer Engineering, University of Toronto, Toronto, Ontario M5S 1A4, Canada

E-mail: pelayo.garciadearquer@icfo.eu; ted.sargent@utoronto.ca

A. R. Kirmani, L. J. Richter

Materials Science and Engineering Division, National Institute of Standards and Technology (NIST), Gaithersburg, MD 20899, USA

P. Li, Z. H. Lu

Department of Material Science and Engineering, University of Toronto, 184 College St, Toronto, ON M5S 3E4, Canada

M. Chekini

Department of Chemistry, University of Toronto, Toronto, Ontario, Canada

This article has been accepted for publication and undergone full peer review but has not been through the copyediting, typesetting, pagination and proofreading process, which may lead to differences between this version and the [Version of Record](#). Please cite this article as [doi: 10.1002/adma.202203039](https://doi.org/10.1002/adma.202203039).

This article is protected by copyright. All rights reserved.

[+] Present address: Key Laboratory for Organic Electronics and Information Displays and Jiangsu Key Laboratory for Biosensors, Institute of Advanced Materials (IAM), Nanjing University of Posts and Telecommunications, Nanjing, 210023 China

Keywords: Photodiode, Near-Infrared, Quantum dots,

Abstract: Colloidal quantum dots (CQDs) are promising materials for IR light detection due to their tunable bandgap and their solution processing; however, to date, the time response of CQD IR photodiodes has been inferior to that provided by Si and InGaAs. We reasoned that the high permittivity of II-VI CQDs leads to slow charge extraction due to screening and capacitance; whereas III-Vs – if their surface chemistry could be mastered – offer a low permittivity and thus increased potential for high-speed operation. In initial studies, we found that the covalent character in InAs leads to imbalanced charge transport, the result of unpassivated surfaces and uncontrolled heavy doping. We report surface management using amphoteric ligand coordination and find that the approach addresses simultaneously the In and As surface dangling bonds. The new InAs CQD solids combine high mobility ($0.04 \text{ cm}^2 \text{ V}^{-1} \text{ s}^{-1}$) with a 4x reduction in permittivity compared to PbS CQDs. The resulting photodiodes achieve a response time faster than 2 ns – the fastest photodiode among previously-reported CQD photodiodes – combined with an external quantum efficiency (EQE) of 30% at 940 nm.

Infrared photodetection underpins applications in medicine and bioimaging, information technology, machine vision, and security^[1, 2]. Emerging technologies such as autonomous driving and augmented reality rely on Light Detection and Ranging (LiDAR) based on time of flight (ToF)^[3]. This requires sensitive and ultrafast photodetection of infrared light with nanoseconds resolution^[4]. Today, this is achieved in the near-infrared (NIR) using indirect bandgap silicon detectors—limited by silicon's low absorption coefficient— and, at longer wavelengths, using epitaxially-grown semiconductors such as III-Vs and $\text{Hg}_{1-x}\text{Cd}_x\text{Te}$ ^[5, 6].

This article is protected by copyright. All rights reserved.

Colloidal quantum dots (CQDs) are of interest given by their low-temperature solution processing, which allows them to be integrated with silicon electronic read-out and signal processing circuitry^[7-10]. Their bandgap is size-tuned over a wide range of wavelengths. PbS, for example, has a widely-programmable absorption onset covering the visible and short-wavelength infrared (SWIR)^[11, 12]; however, its high permittivity, stemming from its ionic character – $\epsilon_r = 180$ for bulk PbS^[13] – slows charge extraction both for bulk^[14] and CQD photodiodes^[15] due to screening and capacitance effects.

Indium arsenide (InAs) CQDs can be tuned in a similar spectral range as PbS CQDs, and offer the prospective advantage of a covalent lattice and hence lower permittivity^[16, 17]. This, however, comes with a challenge: the surface in InAs CQDs is charge-imbalanced, leading to poor passivation and heavy doping, as surface states pin the Fermi level near the conduction band minimum^[18]. Much effort has been paid to improving mobility by decreasing center-to-center distance via ligand exchanges and surface treatments in CQD solids^[19, 20], but III-V CQDs require a new approach to neutralize CQD charge surface states and reduce trap density.

Trap states in InAs semiconductors originate from surface In and As dangling bonds^[21]. Growing epitaxially-matched inorganic shells on CQDs passivates surface defects, but it hinders CQD coupling and carrier transport^[22, 23]. Using molecular metal chalcogenide complexes (MCCs, e.g. $\text{Sn}_2\text{S}_6^{4-}$ and $\text{In}_2\text{Se}_4^{2-}$) enhances carrier mobility in III-V CQD solids, leading to an impressive mobility of $15 \text{ cm}^2\text{V}^{-1}\text{s}^{-1}$, but introduces undesired in-gap states^[20, 24]. Etching As sites using strong acids facilitates In-site passivation but leads to low mobility ($10^{-3} \text{ cm}^2\text{V}^{-1}\text{s}^{-1}$)^[18, 19, 21]. Thiol ligands to replace oleate have been used to passivate As dangling bonds, providing a balanced In:As stoichiometry; but passivation of As alone limits performance, leading to a low EQE (18% at 0 V) and high dark current (a rectification ratio of 7)^[25].

Here we present a surface passivation strategy that addresses charge imbalance and passivation in InAs CQD solids for infrared photodetectors. We introduce InBr_3 passivants to replace native insulating oleic acid ligands, providing surface passivation and charge transport simultaneously. We find that InBr_3 is amphoteric, dissociating into an X-type ligand (Br^-) that passivates In dangling bonds¹⁸; and into a Z-type (InX_2^+) ligand^[26] that passivates As dangling bonds. We incorporate N,N-dimethylformamide (DMF) as a coordinating agent to stabilize otherwise unstable Br^- and InX_2^+ passivants. We demonstrate a charge-balanced CQD surface using a zeta-potential assessment and observe coordination of the DMF. The InBr_3 -InAs CQD solids achieve a mobility value of $0.04 \text{ cm}^2 \text{V}^{-1} \text{s}^{-1}$, >10 times higher than that in halide-exchanged InAs solids^[19], with improved surface passivation. The InBr_3 -InAs CQD solids show a low dielectric constant of ~ 6 – a near 4x advance compared to PbS CQD solid counterparts ($\epsilon_r = \sim 35$). The resultant photodiodes achieve a 30% external quantum efficiency (EQE), a responsivity of 0.22 A W^{-1} , and measured detectivity of $10^{11} \text{ cmHz}^{1/2} \text{W}^{-1}$ at the excitonic peak (940 nm). Transient photocurrent (TPC) experiments reveal a fall time of 2 ns, reaching -3 dB cutoff frequency of 150 MHz. This is the first demonstration of efficient III-V CQD photodiodes, and is the fastest solution-processed infrared photodiode report, with over a 40-fold improvement compared to the best CQDs photodiodes^[15, 27].

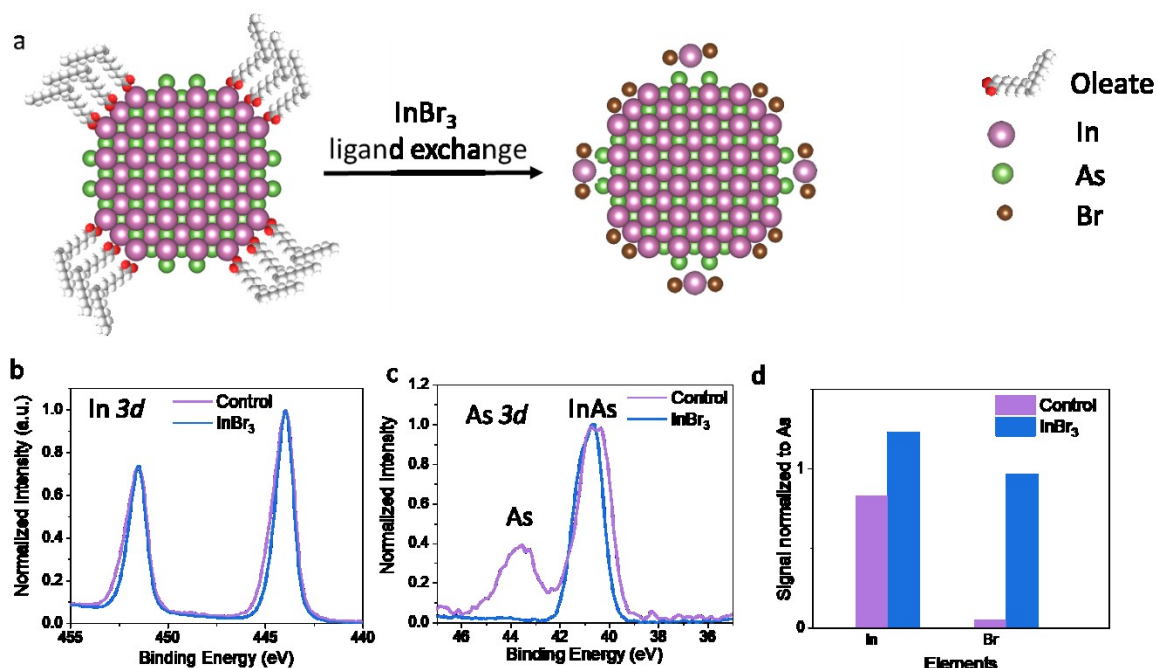


Figure 1 | Stabilization of InAs CQDs. Scheme of InBr_3 ligand exchange and InAs quantum dot surface configuration; b, In 3d X-ray photoelectron spectroscopy (XPS) signal; c, As 3d XPS signal; d, elemental ratio extracted from Rutherford backscattering spectrometry (RBS) measurements of InAs CQD films using InBr_3 ligand exchange and Control exchange.

We first synthesized InAs CQDs (Supporting Information Figure S1) using a continuous injection approach^[28, 29]. As-synthesized InAs CQDs are capped by insulating oleic acid ligands, which need to be removed for electrical coupling. The oleic acid capped InAs (OA-InAs) quantum dots in octane show low photoluminescence quantum yield ($\text{PLQY} < 1\%$)^[28], which we attribute to the presence of surface defects. We note that negatively charged As dangling bonds^[30] are not passivated using oleic acid.

InAs crystal structure is zincblende and the InAs crystal facets exposed are (111), (-1-1-1), (100), and (-100) (Supplemental Figure 2), which are polar and terminated with positively charged In and negatively charged As^[31, 32]. The nature of this structure therefore demands the simultaneous passivation of both In and As dangling bonds that act as traps in CQD solids. Previous studies showed passivation of the positively charged surface using X-type ligands^[30, 31], suggesting that halides could be promising candidates for In passivation. Moreover, during ligand exchange In may leave with oleate ligands from the InAs CQD surface^[32], leaving In vacancies and a more As terminated surface. Z-type ligands binding as a neutral two-electron acceptor (a Lewis acid) have been demonstrated to passivate phosphide on the InP CQD surface, leading to enhanced photoluminescence efficiency^[33]. This prompted us to design a dual passivation strategy that would seek to address In and As dangling bonds using X-type and Z-type ligands, respectively.

We hypothesized that metal halide salts such as InBr_3 could be candidates: when dissolved in certain polar solvents such as DMF, they would dissociate into the needed X-type (Br^-) and Z-type (InBr_2^+) ligands^[26]. The additional In may also contribute to addressing In vacancies. We developed a one-step, two-phase solution exchange to replace OA ligands with InBr_3 salts assisted by ammonium acetate (AA). Before the ligand exchange, InAs CQDs are dispersed in octane and InBr_3 (0.1 mol L^{-1} , 0.18g in 5 mL) and AA (0.04 mol L^{-1} , 0.023g in 5 mL) are pre-dissolved in DMF. During the exchange, InAs CQDs transfer from nonpolar octane layer to polar DMF solution, which indicates that long OA ligands are replaced by InBr_3 based ligands.

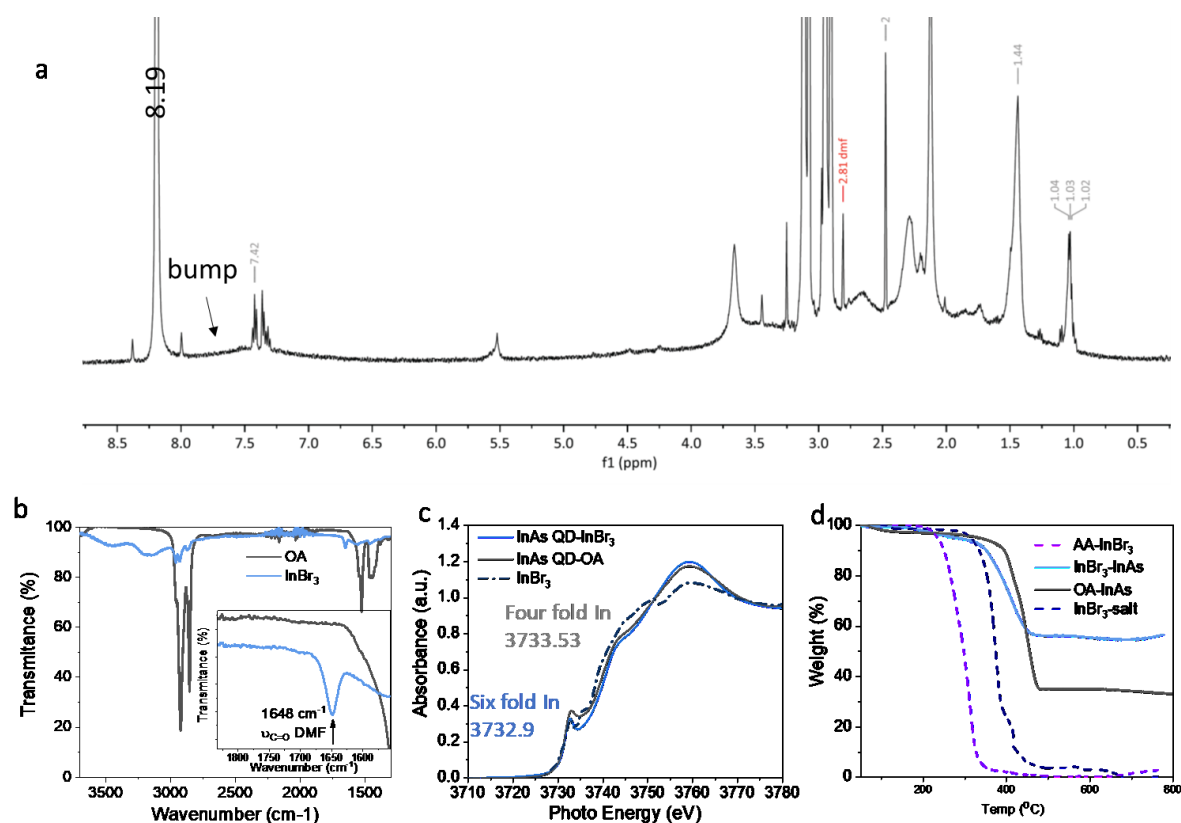


Figure 2 | Investigation of passivation using InBr_3 -DMF complexes. a, ^1H NMR spectrum of InBr_3 -InAs CQDs (50 mg mL^{-1}) in d_6 -DMF (Figure 2b); b, Attenuated total reflection (ATR) FTIR of InAs CQD films before and after InBr_3 ligand exchange on glass. c, In L_3 -edge XANES spectra of InAs CQD films and InBr_3 films (spin-coated from DMF solution) on Si wafer. d, Thermogravimetric analysis (TGA) of InAs CQDs and InBr_3 salt with/without AA samples.

We performed InBr_3 -DMF ligand exchange on OA-capped InAs (OA-InAs) CQDs, and compared with a control exchange (Methods)^[19]. Figure 1b shows the In signal after ligand exchange, where films based on InBr_3 passivated InAs (InBr_3 -InAs) have a narrower peak compared to the Control exchanged InAs CQD film (Control InAs). Figure 1c shows the As signal after ligand exchange without evidence of oxidation on the As, whereas the Control InAs CQD film shows a side peak at 43.5 eV, which belongs to elemental As. We attribute the existence of elemental As to the byproduct of the stripping process. To assess the elemental ratio in the film, we performed RBS measurements. The In-to-As ratio of InBr_3 -InAs is 1.23 (Figure 2c) vs. 0.83 for Control InAs, in agreement with elemental As observed in XPS. This In-to-As ratio larger than 1 we attribute to the introduction of InBr_3 for passivation and addressing In vacancies. The success of Br passivation for InBr_3 -InAs is also confirmed by the Br-to-As ratio of 0.97, whereas Control InAs shows a Br-to-As ratio of only 0.05. We attribute the low Br-to-As ratio to the remaining of BF_4^- ligands on QD surface, and X-type Br^- ligand may not efficiently replace BF_4^- ligands^[19].

To determine whether the DMF forms a complex with InBr_3 salt or acts as complex ligands on the CQD surface, we performed ^1H NMR measurements on InBr_3 -InAs CQDs (50 mg mL^{-1}) in d_6 -DMF (Figure 2b). We observed a resonance feature in the range 8 to 7.5 ppm, close to the peak at 8.19 ppm, the formyl $-\text{CHO}$ proton signal from DMF. The feature may be due to the DMF on CQD surface, when the nanoparticles themselves can create large inhomogeneities in the magnetic field in their local chemical environments^[34]. To investigate this, we measured the InBr_3 salt and Control InAs CQDs in DMF solutions (Supporting Information Figure S3), where no features in the range 8 to 7.5 ppm were observed, indicating that the DMF complexes are on the InBr_3 -InAs CQD surface^[34].

To track the presence of DMF and the removal of long ligands in CQD solids, we carried out Fourier transform infrared spectroscopy (FTIR) measurements (Figure 2b). OA-InAs CQDs show typical CH resonances at $\sim 2900 \text{ cm}^{-1}$ and C=O vibrations owing to the presence of OA on the CQD surface at $\sim 1540 \text{ cm}^{-1}$. After the InBr_3 ligand exchange, the OA signals disappear. The C=O signal at $\sim 1640 \text{ cm}^{-1}$ is attributed to DMF complexes, which differs from the peak position of free DMF at 1675 cm^{-1} ^[35].

To assess the role of the DMF complex, we performed synchrotron (In L_3 -edge) X-ray absorption near edge structures (XANES) (Figure 2c). XANES features of In are not sensitive to anion substitutions, but are sensitive to the coordination number^[36]. InBr₃-InAs films show a similar peak position as pure InBr₃ films deposited from DMF solution, but a shift compared to that of OA-InAs films. The peak position difference suggests that In in InBr₃-InAs and InBr₃ have six-fold coordination (In connects to 6 atoms) whereas OA-InAs only has only fourfold coordination^[36], in agreement with results from ¹H NMR.

We carried out thermogravimetric analysis (TGA) (Figure 2d) to study the stability of InAs CQDs and gain insight into the composition of the final CQD solids. We analyzed the decomposition of ligands and solvent at different temperatures for the exchanged CQDs comparing TGA traces of pure InBr₃, AA-InBr₃, OA-InAs, and InBr₃-InAs: the weight loss of 1% in the range from 50°C to 158°Cs attributed to the free DMF solvent (boiling point 153°C) in InBr₃-InAs solids; the weight loss of ≈2.5% in the range from 162°C to 240°Cs attributed to the DMF from the decomposition of DMF-InBr₃ complex; the weight loss of ≈3.5% in the range from 240°C to 340°C may be decomposition of the AA/InBr₃ complex (similar to the decomposition of AA-InBr₃); the final weight loss of ≈36.5% from 340°C to 420°Cs attributed to the decomposition of InBr₃. We then converted this weight loss to the atomic ratio (Supporting Information Table S 1), and found an In-to-As ratio to be 1.37 and a Br-to-As ratio to be 1.1, about 10% higher than the values extracted from RBS. We attribute this difference to residual oleic acid on the CQD surface. The decomposition of the DMF-InBr₃ complex agrees with the InBr₃-DMF co-passivation mechanism^[37].

We characterized the absorption of CQDs in solution before and after the ligand exchange (Figure 3a). OA-capped CQDs show an excitonic peak at 916 nm with a peak-to-valley ratio of ≈2.6. After ligand exchange, the excitonic peak redshifts to 928 nm and the peak-to-valley ratio decreases to ≈2.2, indicating that the ligand exchange avoids etching of InAs CQDs^[19, 25, 38].

To assess the effectiveness of passivation, we qualified the effective electric charge on the CQD surface in DMF using electron kinetic potential (zeta-potential) measurement. The Control InAs CQDs in DMF solution show a positive zeta-potential of 35 ± 1.5 mV, agreeing with the In-rich surface^[19], where the large zeta-potential indicates the well-dispersed CQD solution. In contrast, InBr₃-InAs CQD surface gained simultaneous passivation, exhibiting a near-neutral zeta-potential, -2.2 ± 0.6 mV, and we hypothesize that the DMF complexes on CQD surface act as stabilizer for the CQD solution with the charge-neutral surface (Figure 3b).

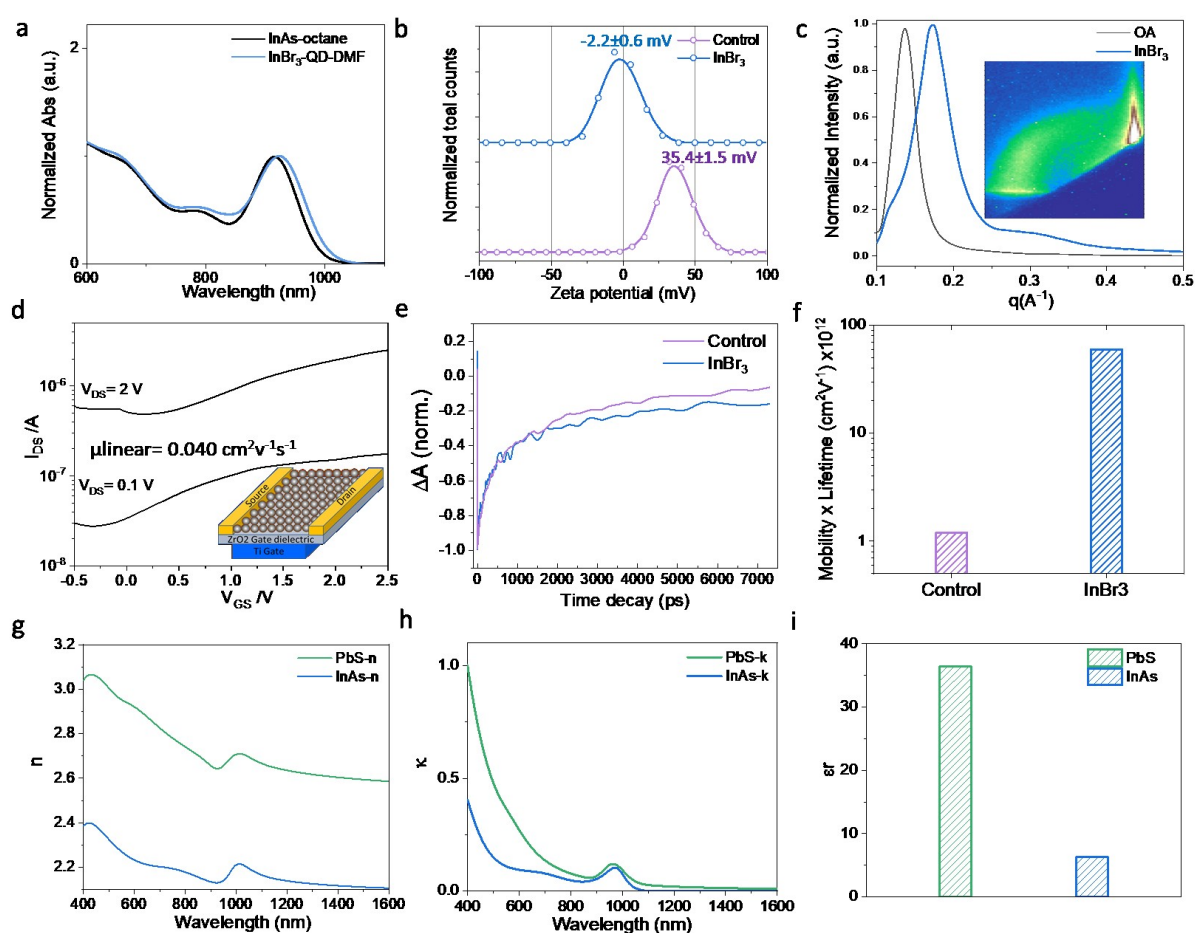


Figure 3 | Optoelectronic characterization of InBr₃-InAs CQD films. **a**, Absorption of InAs CQD solution before and after ligand exchange. **b**, zeta-potential of InAs CQDs (2mg mL⁻¹ in DMF) using InBr₃ ligand exchange and Control exchange; **c**, Azimuthal integration of (GISAXS) patterns of InAs CQD films with GISAXS 2D pattern (inset) of InBr₃-InAs CQD film. **d**, Transfer curves of InBr₃-InAs CQD film in linear and saturation regimes with the field-effect transistor (FET) device structure (inset). **e**, decay kinetics and **f**, mobility $\mu \times$ lifetime t product of InBr₃-InAs and Control InAs CQD films; **g**, The real and **h**, Imaginary refractive index of InAs compared to PbS QDs. **i**, Dielectric constant of InBr₃-InAs and Pbl₂-PbS CQD films.

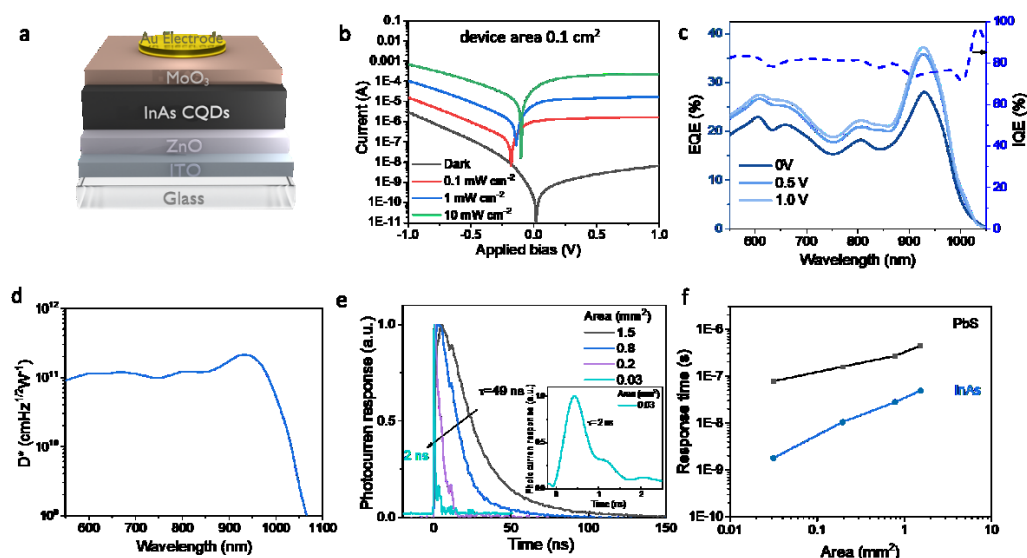
To assess the interparticle distance and the necking produced in films after ligand exchange, we carried out grazing-incidence small-angle X-ray scattering (GISAXS) (Figure 3c). After InBr₃ ligand exchange, the center-to-center distance decreased from 4.6 nm to 3.6 nm, as extracted from the azimuthally integrated coherence peak. This is consistent with OA replacement by inorganic ligands.

To characterize charge transport in the exchanged CQD solid, we measured mobility using FETs^[39]. FET output characteristics reveal n-type transport enhancement mode for InBr₃-InAs CQD films (Supporting Information Figure S4). The carrier mobility is $0.032 \pm 0.003 \text{ cm}^2 \text{V}^{-1} \text{s}^{-1}$ in the linear regime (μ_{lin}) and $0.040 \pm 0.005 \text{ cm}^2 \text{V}^{-1} \text{s}^{-1}$ in the saturation regime (μ_{sat}) is, (Figure 3d), more than 10 times higher than that of the two-step ligand exchange, $0.00063 \pm 0.00016 \text{ cm}^2 \text{V}^{-1} \text{s}^{-1}$ in the saturation regime. (Supporting Information Figure S5)^[19]. The current on/off ratio is about 10, indicating that the thickness of the CQD layer exceeded the depth of the accumulation channel formed in the CQD solid upon applied gate bias and that the electron concentration is high in InBr₃-InAs CQD solids.

We extracted the carrier concentration through mobility and conductivity, obtaining a value of $1.1 \times 10^{17} \text{ cm}^{-3}$ and $1.4 \times 10^{17} \text{ cm}^{-3}$ from μ_{lin} and μ_{sat} , respectively. This suggests that the InBr₃-InAs CQD solids are n-type doped. We confirmed the n-type transport polarity of InBr₃-InAs CQD films using ultraviolet photoelectron spectroscopy (UPS), which revealed a conduction band minimum (CBM) at -4.62 eV, a valence band maximum (VBM) at -5.92 eV, and a Fermi level (E_F) at -4.79 eV (Supporting Information Figure S6a, b). This agrees with the carrier concentration obtained from FET results.

To assess the passivation, we obtained carrier lifetimes of InBr_3 -InAs and Control InAs CQD films using a nanosecond TA setup (Figure 3d, 3e). We extracted the carrier life time from the kinetics, and each decay trace was fit to a biexponential curve (Supporting Information Figure S7), where the lifetimes of InBr_3 -InAs and Control InAs CQD films were found to be 1500 ± 200 ps and 1900 ± 200 ps (Supporting Information Table S 2), respectively. When combined with the mobility, the InBr_3 -InAs film shows fully a 70-fold higher mobility-lifetime product (Figure 3f) compared to the Control InAs CQD film, indicating improved surface passivation.

To assess the optical properties of exchanged InAs films, we measured the complex refractive index and compared it with that of PbS CQD films for reference. We found that the real part of the refractive index is higher in PbS CQD films (Figure 3g, 3h), consistent with the material's higher permittivity. To characterize the dielectric constant at electrical frequencies, we measured the capacitance in a diode device configuration (Supporting Information Figure S8 and Figure 3i). We obtained $\epsilon_r = 35$ for PbS and $\epsilon_r = 6$ for InAs CQD solids.



Figure

4 | Photodetector using low- ϵ InAs CQDs. **a**, Schematic of photodiode device structure. **b**, I - V characteristics of InBr₃-InAs CQD photodiodes dark and illuminated condition. **c**, External quantum efficiency (EQE) biased from 0 to 1 V and internal quantum efficiency (IQE, divide EQE (@ 0 V) by EQE (@ 1 V)). **d**, Detectivity of InBr₃-InAs CQD photodiodes. **e**, Device-area-dependent response time of InBr₃-InAs CQD photodiodes. **f**, Comparison of the response time of devices with InAs CQD and PbS CQD films (same thickness 120 \pm 5 nm, same device structure: ITO/ZnO/CQDs/MoO₃/Au) with different device areas.

We then moved to fabricate InAs CQD-based photodiodes. Considering the energy levels of InAs CQD solids, we designed a device architecture consisting of ITO / ZnO / InAs / Au. Unfortunately, this arrangement resulted in poor diode behavior and high dark currents (Supporting Information Figure S9a). Reasoning that this structure may have produced back injection of electrons from InAs into Au, we added a layer of 10 nm of MoO₃ as an electron blocking layer between InAs and Au (Figure 4a, Supporting Information Figure S6b)^[40]. We observed a decrease in dark current by 3 orders magnitude to ≈ 700 nA cm⁻² at 1.0 V reverse bias (Figure 4b) accompanied by an increase in EQE from 9% to 30% at 0 V bias (Figure 4c), a responsivity of 0.22 A W⁻¹ (Supporting Information Figure S10) and measured detectivity of 10¹¹ cmHz^{1/2}W⁻¹ at the excitonic peak (940 nm, Figure 4d). This is the highest EQE reported for an InAs CQD photodetector. To study charge extraction and the impact of energy levels on device performance, we carried out SCAPS^[41, 42] simulations, which reveal the

presence of a small barrier at the ETL/active layer interface (Supporting Information Figure S6c). We conclude that the band alignment between ZnO and InAs is not optimal for device operation, but does not prevent charge extraction. Future studies could seek to improve band alignment and charge extraction in InAs CQD devices. We also evaluated the Control-InAs on the same device structure (ITO/ZnO/Control-InAs/MoO₃/Au), and found a much lower EQE of 4% at 0 V bias (Supporting Information Figure S11a), which we attribute to a lower carrier mobility $\mu \times$ lifetime product.

We then characterized the time response of the InAs CQD photodiodes without external bias after ultrafast photoexcitation using 100 fs laser pulses. The response time (τ_r) is determined by three components: the RC time constant (τ_{RC} , corresponding to the time it takes to charge/discharge the capacitors in the electrical circuit), the drift of charge carriers in the space-charge region (τ_{drift}), and the diffusion of charge carriers in the charge-neutral region $\tau_{diff}^{[27, 43]}$ (Supporting Information). When the depletion region is thicker than the active layer, the response time is dominated by τ_{RC} and τ_{drift}^{43} . To assess τ_{RC} , we studied the response time for different pixel areas (Supporting Information Figure S12). The fall time decreases from 50 ns for 1.5 mm² to 2 ns for 0.03 mm² pixels (Figure 4e) at 0 V. Our analysis shows that, for all areas considered herein, the geometrical capacitance is the determinant of temporal response in the InAs devices, and we may obtain a shorter response time in a smaller device^[44].

PbS CQD devices in Figure 4e show a similar trend, but with a near two orders of magnitude longer fall time compared to InAs diodes (Figure 4f). Supporting Information Figure S13a shows that there is a large difference between the calculated and measured response time for PbS CQD devices, both in the trend (slope of the line) and in the absolute numbers. This difference suggests that, in the case of PbS, the geometrical capacitance is not the only speed limiter, particularly for smaller device areas. The ionic nature of the Pb-S bond in the dots or Pb-halide salts in the exchange process; ionic, orientational; space charge polarization; and different interfaces, could be other contributing factors.

We then measured the 3 dB cut-off frequency with the aid of a vertical-cavity surface-emitting laser (VCSEL) light source modulated at different frequencies (Supporting Information Figure S15).

The response stays constant until 25 MHz and crosses -3 dB at about 150 MHz (Figure 4f). This is in agreement with TPC results for the same diameter pixel (0.03 mm^2), which reveal a fall time of 2 ns corresponding to a 3 dB cut-off frequency of $\approx 175 \text{ MHz}$.

In sum, we have introduced an amphoteric dual passivation strategy that passivates both In and As sites on InAs CQD surfaces that provides passivation and charge transport for low permittivity CQD solids. We found the important role of DMF as a coordinating agent that stabilizes the passivants and the CQD surface. Consequently, we were able to achieve for the first time efficient InAs CQDs photodiodes showcasing an EQE of $\sim 30\%$ at 0 V and a specific detectivity of $10^{11} \text{ cmHz}^{1/2}\text{W}^{-1}$ at the near-infrared. The low permittivity and good carrier transport in InAs result in a fall time of 2 ns – the fastest CQD photodiodes reported to date.

Experimental Section/Methods

Materials: All the chemicals are purchased from commercial suppliers and used as received. Suppliers disclaimer: “Certain commercial equipment, instruments, or materials are identified in this paper to specify the experimental procedure adequately. Such identification is not intended to imply recommendation or endorsement by the National Institute of Standards and Technology, nor is it intended to imply that the materials or equipment identified are necessarily the best available for the purpose.”

InAs CQDs Synthesis: InAs QDs were synthesized using a modified approach via the continuous injection by reacting In(oleate)_3 , tris(trimethylgermyl)arsine ($(\text{TMGe})_3\text{As}$) under an N_2 atmosphere at 300°C using a modified approach^[28, 29].

Control (Two step) InAs ligand exchange: 50 mg of InAs CQDs in 1 mL of octane are mixed with 3-mL solution of NOBF_4 , 0.02 M in DMF. CQDs transfer to DMF phase after 2 min Vortex. The colorless octane phase is discarded followed by 3 times of wash with pure octane. The pure toluene was added to precipitate the CQDs in DMF phase and centrifuged at 6k rpm for 4 min. The precipitate is re-dispersed in 2 mL of DMF. 5 mL of toluene is added and centrifuged at 6000 rpm for 4 min. The precipitate is then dried in vacuum for overnight. The final produce is redispersed in 2 mL

of DMF followed by mixing with 5 mL of 0.01% ammonium bromide (NH_4Br) in anhydrous MeOH. After vortexing for 2 min, toluene is employed to precipitate the CQD, which is followed by centrifugation at 6000 rpm for 4 min. The final product is dried in vacuum for 2 h before being redispersed in DMF.

Zeta(ζ)-potential measurements: All electrophoretic mobility data were collected using a Zetasizer Nano-ZS system (Malvern Instruments). CQD solutions were put into quartz cuvettes with dip cell electrodes and then inserted into the instrument stage. All measurements include 100 scans and all measurements were repeated at least three times. QD colloids were diluted to concentrations (about 2 mg mL⁻¹) that gave the best signal-to-noise ratio. The ζ potentials were obtained by using Henry's equation and the Hückel approximation for non-polar systems:

$$\frac{U}{E} = \frac{2\varepsilon \zeta F(\kappa a)}{3\eta} \quad (1)$$

where U/E is the electrophoretic mobility obtained using the instrument, ζ is the ζ potential, ε is the solvent dielectric permittivity, η is the viscosity and $F(\kappa a)$ is the dimensionless Henry function. For non-polar systems, the Hückel approximation is applied and the value of Henry's function is close to 1. The mobility data for ζ -potential measurements in Figure 3b.

Fabrication of PbS CQD devices: The ITO glass substrates were cleaned by sonication in acetone and isopropanol for 30 min each. After drying, the ZnO nanoparticle via sol-gel method using Zinc acetate dihydrate ($\text{Zn}(\text{CH}_3\text{COO})_2 \cdot 2\text{H}_2\text{O}$) as a precursor in ethanol ($\text{CH}_3\text{CH}_2\text{OH}$) and spin-coated onto ITO glass substrates at 2000 rpm for 30 s, followed by 340 °C annealing in air for 40 min. CQD synthesis and solution ligand exchange. PbS CQDs were synthesized and washed according to previous reports.^[45] A ligand-exchange process was carried out in the solution phase in air ambient. The exchange solution was prepared (PbI_2 0.1 M PbBr_2 0.04 M and ammonium acetate (AA) 0.04 M) in DMF. 5 ml of as-synthesized PbS CQDs octane solution (10 mg mL⁻¹) were added to 5 ml of precursor solution, followed by vigorous mixing for 2 min until the CQDs completely transferred to the DMF phase. The DMF phase was then washed three times with octane, followed by adding 3 mL of toluene and centrifuging to collect precipitates. Then the solids were dried for 15 min in vacuum.

1) The dried CQD solids were redispersed in butylamine (BTA) ($200\text{--}350\text{ mg mL}^{-1}$) for film by spin coating at a spin rate from 1500 to 2500 RPM in air, followed by annealing at 70°C for 15 min in N_2 filled glovebox to remove solvent residues. . The photodetector was finalized by sequential deposition of 10 nm of MoO_3 and 120 nm of Au that serves as the top electrode. 2) EDT-exchanged PbS CQD layer as hole transport layer was also evaluated as follows: 50 μL of oleic acid-capped PbS CQDs (exciton peak at 850 nm) octane solution (50 mg mL^{-1}) were spin-coated on the dried PbI_2 exchanged PbS CQD film at 2500 rpm for 10 s, followed by soaking in 0.01% EDT in ACN (ACN) solution for 30 s and washing with ACN for 3 times. Then 120 nm of Au was deposited on EDT PbS CQD film as a back electrode. The photodetector area was described in Supporting Information Figure S11.

InAs CQD device fabrication: The InBr_3/AA solution-phase ligand-exchange process was carried out in a test tube in an N_2 -filled glovebox. InBr_3 (0.1 mol L^{-1} , 0.18g) and ammonium acetate (0.04 mol L^{-1} , 0.023g) are pre-dissolved in 5 mL of dimethylformamide (DMF). A 5 ml amount of CQD octane solution (10 mg mL^{-1}) was added to 5 ml of the precursor solution. These were vortexed for 1–2 min until the CQDs completely transferred to the DMF phase, followed by washing three times with octane. After ligand exchange, CQDs were precipitated via the addition of toluene ($\sim 10\text{ mL}$) and separated by centrifugation. After 10 min of vacuum drying, the CQDs were then redispersed in DMF (200 mg mL^{-1}) to form the film on ZnO nanoparticle coated ITO substrate by spin-coating at (1000 to 2000) rpm. Finally, 100 nm of Au was thermally deposited as a back electrode.

X-Ray Photoelectron Spectroscopy (XPS): XPS spectra were measured in N_2 by using a Thermo Scientific K-Alpha System with an Al $\text{K}\alpha$ source. The films were spin-coated on Si substrates. Scans were taken in 0.05 eV steps with a 50 eV pas energy. The atomic ratios were obtained by integrating under the area of each peak and scaled by atomic sensitivity factors. We normalized all of the element areas to As to obtain accurate atomic ratios.

Fourier transform infrared (FTIR) spectroscopy measurements: FTIR measurements were performed on a Bruker Vertex 80, ($8000\text{ to }600\text{ cm}^{-1}$; resolution 4 cm^{-1} , in top-configuration (attenuated total reflection, ATR).

Absorption Measurements: The optical absorption measurements were performed with a Perkin-Elmer Lambda 950 UV-Vis-NIR spectrophotometer. The solutions were placed in a quartz cuvette with a 1 mm path length.

Transmission electron microscopy measurements (TEM): TEM images were acquired on a Hitachi HF 3300 electron microscope operating at 300 keV. TEM samples were prepared by drop-casting a purified solution of CQDs from n-octane onto a 300 mesh copper grid with a carbon film (SPI supplies).

X-ray scattering measurements: Grazing incidence small-angle X-ray scattering (GISAXS) samples were prepared by spin-coating a layer of InAs film following the same procedure as the device fabrication on a Si substrate. The measurements were carried out at the CMS beamline of the National Synchrotron Light Source II, a U.S. Department of Energy (DOE) office of the Science User Facility operated for the DOE Office of Science by Brookhaven National Laboratory. GISAXS images were collected with an imaging detector at a distance of 0.178 m using X-ray wavelength of 1.033 Å. Nika software package was used to sector average the 2D GISAXS images. Data plotting was done in Igor Pro (Wavemetrics, Inc., Lake Oswego, OR, USA).

Thermal gravimetric analysis measurement (TGA): TGA measurements were conducted using a PerkinElmer Pyris 1 TGA. About (6 to 8) mg of quantum dot solids were taken on a platinum pan. An equilibration or isothermal step at 50 °C for 15 min and later heated to 800 °C with a heating rate of 10°C/min were carried out under nitrogen. The residual weight of InAs QDs after 780°C increased from 37% to 56% after ligand exchange, which confirms the reduced amount of organic ligands as OA was replaced. We also analyzed the decomposition of ligands and solvent at different temperatures for the exchanged CQDs comparing TGA traces of pure InBr₃, AA-InBr₃, OA-InAs, and InBr₃-InAs: The weight loss of 1% in the range from 50 °C to 158 °C attributed to the free DMF solvent (boiling point 153 °C) in InBr₃-InAs solids; the weight loss of ≈2.5 % in the range from 162 °C to 240 °C attributed to the DMF from the decomposition of DMF-InBr_x complex; the weight loss of ≈3.5% in the range from 240 °C to 340 °C may be the AA/InBr₃ complex decomposition (similar to the decomposition of AA-InBr₃); the final weight loss of ≈36.5% from 340 °C to 420 °C attributed to the decomposition of InBr₃ and residual OA.

Refractive indexes: The CQD films were spincoated on c-Si substrate with a thermally grown 100 nm-SiO₂ layer. We performed ellipsometry measurements using J. A. Woollam M-2000 ellipsometer and extracted the refractive indexes of the CQD films. The model used to fit the spectroscopic ellipsometry data taken on all CQD films were air/surface roughness/CQDs/SiO₂/c-Si. The surface roughness was modeled using a Bruggeman effective medium approximation^[46]. The optical functions of CQD films were extracted by fitting with Tauc-Lorentz model^[47].

Transient absorption measurements: Femtosecond laser pulses were produced using a regeneratively amplified Yb:KGW laser (PHAROS, Light Conversion), with a 1030 nm fundamental wavelength at a 5 kHz repetition rate. A portion of the fundamental was used to pump an optical parametric amplifier (ORPHEUS, Light Conversion), generating the pump beam at 400 nm. Both the pump and residual fundamental were directed into a commercial transient absorption spectrometer (Helios, Ultrafast). The fundamental was passed through a delay stage (up to 8 ns delay) and then focused into a sapphire crystal, generating the white light continuum probe beam. The pump beam was sent through a mechanical chopper, reducing its repetition rate to 2.5 kHz. The time resolution of these experiments was ~200 to 300 fs (estimated by the rise time of the transient absorption signals). All measurements were performed using an average power of ~50 μ W with a spot size of 0.4 μ m².

FET fabrication: Bottom-gate top-contact FET configuration is used as follows: 70 nm of titanium (Ti) gate was thermally evaporated onto a glass substrate, followed by 15 nm of ZrO₂ as a dielectric layer using atomic layer deposition (ALD). After 300°C baking for 1 hour, the pre-exchanged InAs CQDs dissolved in DMF was spin-coated onto the substrate. Then 70 nm of Au source/drain electrodes were thermally deposited using an Angstrom Engineering Amod deposition system. Agilent semiconductor analyzer was used to characterize the FET devices. We calculated carrier mobility from the slope of the drain-source current (I_{DS}) vs. gate voltage (V_{GS}) according to the equation $I_{DS} = \frac{\mu_{lin} C_i W}{L} (V_{GS} - V_{TH}) V_{DS}$ (2) and $I_{DS} = \frac{\mu_{sat} C_i W}{2L} (V_{GS} - V_{TH})^2$ (3), where μ_{lin} and μ_{sat} are the carrier mobility in the linear regime and saturation regime, respectively; I_{DS} is the drain-source

current; L and W are the channel length (50 μm) and channel width (2.5 mm) respectively; C_i is the capacitance per area (450 nF cm^{-2}), and V_{GS} and V_{TH} are the gate voltage and threshold voltage, respectively. We also obtained the carrier density following the formula

$$\sigma = L/(R A) \quad (3) \text{ and } n = \sigma/(q \mu) \quad (4)$$

where σ is the conductivity; L is channel length; R is the resistance of the device; A is the cross area of the film between source and drain electrodes; n is the carrier concentration (electron concentration in this test); q is the elementary charge; μ is the mobility.

Ultraviolet photoelectron spectroscopy (UPS) measurement: A CQD film on indium tin oxide (ITO) glass on was measured in a PHI5500 Multi-Technique system with a base pressure of $\sim 10^{-9}$ Torr and the Fermi energy calibrated to 0 eV. A helium discharge source (HeI α , $h\nu = 21.22$ eV) was used and the samples were kept at a take-off angle of 88° . During measurement, the sample was held at a -15 V bias relative to the spectrometer to efficiently collect low-kinetic energy electrons. Fermi level (E_F) was calculated from the equation: $E_F = 21.22 \text{ eV} - \text{SECO}$, where SECO is the Secondary Electron Cut-off. The difference between VBM level and Fermi level, η , was determined from VBM onset in the VBM region ^[48].

Photodiode fabrication: The ITO glass substrates were cleaned by sonication in acetone and isopropanol for 30 min each. After drying, the ZnO nanoparticle via sol-gel method using Zinc acetate dihydrate ($\text{Zn}(\text{CH}_3\text{COO})_2 \cdot 2\text{H}_2\text{O}$) as a precursor in ethanol ($\text{CH}_3\text{CH}_2\text{OH}$) and spin-coated onto ITO glass substrates at 2000 rpm for 30 s, followed by 340°C annealing in air for 40 min. Then InBr_3 - InAs CQDs in DMF (200mg mL^{-1}) was spin-coated on the substrate. The photodetector was finalized by sequential deposition of 10 nm of MoO_3 and 120 nm of Au that serves as the top electrode. The photodetector area was described in Supporting Information Figure S11.

External and Internal Quantum Efficiency: EQE and IQE spectra were acquired on a QuantX-300 quantum efficiency measurement system (Newport). Monochromated white light from a xenon lamp was mechanically chopped at a frequency of 25 Hz. EQE spectra were acquired at zero

electrical bias, whereas IQE spectra were calculated from EQE spectra taken at a negative bias of -1 V using the following formula: $\text{IQE} = \text{EQE}(0\text{V}) / \text{EQE}(-1\text{V})$ (5).

Noise measurement: Noise spectra were acquired using a signal analyzer (Agilent N9010A). The measured noise level at 500 kHz after 10^7 V/A amplification (using low noise transimpedance preamplifier, FEMTO DHPA-100N9010A), is shown in Figure S10b. The electrical bandwidth of the noise measurement was set to 1 Hz. From these data, the noise spectral density (NSD, $\text{A}/\sqrt{\text{Hz}}$) is directly calculated.

To calculate the NEP (noise equivalent power), we divided the noise spectral density by the detector responsivity (A/W). The specific detectivity was calculated using the equation below:

$$D^* = \sqrt{\text{Detector area}} / \text{NEP} \quad \left[\frac{\text{cm} \sqrt{\text{Hz}}}{\text{W}} \right] \quad (5)$$

The resulting experimental specific detectivity for InAs devices is shown in Figure 4d.

Time response measurements: Transient photocurrent (TPC) measurements were performed with a 26 GHz SG radiofrequency probe (T26A - MPI corporation) with 1000-micrometer pitch. The probe was connected with a fast SMA cable directly to the 50-ohm input of an oscilloscope (16 GHz Agilent DSAX91604A Infiniium). 150 femtosecond laser pulses at a 5 kHz repetition rate were produced using a regeneratively amplified Yb:KGW laser (PHAROS, Light Conversion). The electrical output signal from the fs laser system was used to trigger the oscilloscope. All reported experiments were done using a 850 nm excitation without external bias across the device. We did not observe changes in the response time with application of external bias, indicative of an RC-limited time response.

Supporting Information

Supporting Information is available from the Wiley Online Library or from the author.

Acknowledgements

B. Sun, A. Morteza Najarian, L. Kishore Sagar, M. Biondi, M.-J. Choi contributed equally to this work. We acknowledge funding from NSERC Discovery Grant and Canada Research Chair. This research used resources of the National Synchrotron Light Source II, which is a U.S. Department of Energy (DOE) Office of Science Facility, operated at Brookhaven National Laboratory under contract no. DESC0012704.

Received: ((will be filled in by the editorial staff))

Revised: ((will be filled in by the editorial staff))

Published online: ((will be filled in by the editorial staff))

The table of contents entry should be 50–60 words long and should be written in the present tense. The text should be different from the abstract text.

F. P. García de Arquer and E. H. Sargent Corresponding Author*

References

- [1] J. Caniou, "Passive Infrared Detection: Theory and Applications", 2010.
- [2] C. L. Tan, H. Mohseni, **2018**, 7, 169.
- [3] M. Hansard, S. Lee, O. Choi, R. P. Horaud, *Time-of-Flight Cameras: Principles, Methods and Applications*, Springer-Verlag London, 2011.
- [4] J. Hasch, "Driving towards 2020: Automotive radar technology trends", presented at *2015 IEEE MTT-S International Conference on Microwaves for Intelligent Mobility (ICMIM)*, 27-29 April 2015, 2015.
- [5] A. Rogalski, *Opto-Electron. Rev.* **2012**, 20, 279.

This article is protected by copyright. All rights reserved.

- [6] T. Suzuki, "Challenges of image-sensor development", presented at *2010 IEEE International Solid-State Circuits Conference - (ISSCC)*, 7-11 Feb. 2010, 2010.
- [7] C. R. Kagan, E. Lifshitz, E. H. Sargent, D. V. Talapin, *Science* **2016**, 353.
- [8] M. V. Kovalenko, *Nat. Nanotechnol.* **2015**, 10, 994.
- [9] D. J. Norris, *Nat. Photonics* **2019**, 13, 230.
- [10] A. R. Kirmani, J. M. Luther, M. Abolhasani, A. Amassian, *ACS Energy Letters* **2020**.
- [11] R. Saran, R. J. Curry, *Nat. Photonics* **2016**, 10, 81.
- [12] S. A. McDonald, G. Konstantatos, S. Zhang, P. W. Cyr, E. J. Klem, L. Levina, E. H. Sargent, *Nat. Mater.* **2005**, 4, 138.
- [13] E. Burstein, S. Perkowitz, M. Brodsky, "The Dielectric Properties Of The Cubic Iv-Vi Compound Semiconductors", 1968.
- [14] H. Zogg, S. Blunier, T. Hoshino, C. Maissen, J. Masek, A. N. Tiwari, *IEEE Trans. Electron Devices* **1991**, 38, 1110.
- [15] J. P. Clifford, G. Konstantatos, K. W. Johnston, S. Hoogland, L. Levina, E. H. Sargent, *Nat. Nanotechnol.* **2009**, 4, 40.
- [16] K. Qiao, H. Deng, X. Yang, D. Dong, M. Li, L. Hu, H. Liu, H. Song, J. Tang, *Nanoscale* **2016**, 8, 7137.
- [17] H. Fang, W. Hu, P. Wang, N. Guo, W. Luo, D. Zheng, F. Gong, M. Luo, H. Tian, X. Zhang, C. Luo, X. Wu, P. Chen, L. Liao, A. Pan, X. Chen, W. Lu, *Nano Lett.* **2016**, 16, 6416.
- [18] H. Fu, A. Zunger, *Phys. Rev. B* **1997**, 56, 1496.
- [19] J. H. Song, H. Choi, H. T. Pham, S. Jeong, *Nat. Commun.* **2018**, 9, 4267.
- [20] W. Liu, J. S. Lee, D. V. Talapin, *J. Am. Chem. Soc.* **2013**, 135, 1349.
- [21] Y. Kim, J. H. Chang, H. Choi, Y. H. Kim, W. K. Bae, S. Jeong, *Chem. Sci.* **2020**, 11, 913.
- [22] W. K. Bae, L. A. Padilha, Y.-S. Park, H. McDaniel, I. Robel, J. M. Pietryga, V. I. Klimov, *ACS Nano* **2013**, 7, 3411.
- [23] M. J. Speirs, D. M. Balazs, H. H. Fang, L. H. Lai, L. Protesescu, M. V. Kovalenko, M. A. Loi, *J. Mater. Chem. A* **2015**, 3, 1450.
- [24] E. Scalise, V. Srivastava, E. Janke, D. Talapin, G. Galli, S. Wippermann, *Nat. Nanotechnol.* **2018**, 13, 841.
- [25] M.-J. Choi, L. K. Sagar, B. Sun, M. Biondi, S. Lee, A. M. Najjariyan, L. Levina, F. P. García de Arquer, E. H. Sargent, *Nano Letters* **2021**, 21, 6057.
- [26] N. Kirkwood, J. O. V. Monchen, R. W. Crisp, G. Grimaldi, H. A. C. Bergstein, I. du Fossé, W. van der Stam, I. Infante, A. J. Houtepen, *J. Am. Chem. Soc.* **2018**, 140, 15712.
- [27] Q. Xu, L. Meng, K. Sinha, F. I. Chowdhury, J. Hu, X. Wang, *ACS Photonics* **2020**, 7, 1297.
- [28] L. K. Sagar, G. Bappi, A. Johnston, B. Chen, P. Todorović, L. Levina, M. I. Saidaminov, F. P. García de Arquer, S. Hoogland, E. H. Sargent, *Chem. Mater.* **2020**, 32, 2919.
- [29] S. Tamang, S. Lee, H. Choi, S. Jeong, *Chemistry of Materials* **2016**, 28, 8119.
- [30] O. I. Mičić, J. Sprague, Z. Lu, A. J. Nozik, **1996**, 68, 3150.
- [31] C. L. Hartley, J. L. Dempsey, *Nano Lett.* **2019**, 19, 1151.

- [32] J.-H. Ko, D. Yoo, Y.-H. Kim, *Chemical Communications* **2017**, 53, 388.
- [33] J. L. Stein, E. A. Mader, B. M. Cossairt, *J. Phys. Chem. Lett.* **2016**, 7, 1315.
- [34] H. Yamamoto, H. Yano, H. Kouchi, Y. Obora, R. Arakawa, H. Kawasaki, *Nanoscale* **2012**, 4, 4148.
- [35] Y.-K. Ren, S.-D. Liu, B. Duan, Y.-F. Xu, Z.-Q. Li, Y. Huang, L.-H. Hu, J. Zhu, S.-Y. Dai, *J. Alloys Compd.* **2017**, 705, 205.
- [36] J. T-Thienprasert, S. Rujirawat, J. Nukeaw, S. Limpijumnong, *Comput. Mater. Sci.* **2010**, 49, S37.
- [37] A. Dong, X. Ye, J. Chen, Y. Kang, T. Gordon, J. M. Kikkawa, C. B. Murray, *J. Am. Chem. Soc.* **2011**, 133, 998.
- [38] J. Choi, M. J. Choi, J. Kim, F. Dinic, P. Todorovic, B. Sun, M. Wei, S. W. Baek, S. Hoogland, F. P. Garcia de Arquer, O. Voznyy, E. H. Sargent, *Adv. Mater.* **2020**, 32, e1906497.
- [39] B. Sun, O. Voznyy, H. Tan, P. Stadler, M. Liu, G. Walters, A. H. Proppe, M. Liu, J. Fan, T. Zhuang, J. Li, M. Wei, J. Xu, Y. Kim, S. Hoogland, E. H. Sargent, *Adv. Mater.* **2017**, 29, 1700749.
- [40] R. Singh, S. R. Suranagi, M. Kumar, V. K. Shukla, *J. Appl. Phys.* **2017**, 122, 235302.
- [41] M. Burgelman, P. Nollet, S. Degrave, *Thin Solid Films* **2000**, 361-362, 527.
- [42] M. Burgelman, K. Decock, S. Khelifi, A. Abass, *Thin Solid Films* **2013**, 535, 296.
- [43] A. Goushcha, B. Tabbert, *Opt. Eng.* **2017**, 56, 097101.
- [44] J. Gao, S. C. Nguyen, N. D. Bronstein, A. P. Alivisatos, *ACS Photonics* **2016**, 3, 1217.
- [45] Z. Ning, O. Voznyy, J. Pan, S. Hoogland, V. Adinolfi, J. Xu, M. Li, A. R. Kirmani, J.-P. Sun, J. Minor, K. W. Kemp, H. Dong, L. Rollny, A. Labelle, G. Carey, B. Sutherland, I. Hill, A. Amassian, H. Liu, J. Tang, O. M. Bakr, E. H. Sargent, *Nat. Mater.* **2014**, 13, 822.
- [46] D. A. G. Bruggeman, *Annalen der Physik* **1935**, 416, 636.
- [47] A. S. Keita, A. E. Naciri, F. Delachat, M. Carrada, G. Ferblantier, A. Slaoui, *J. Appl. Phys.* **2010**, 107, 093516.
- [48] B. Lüssem, M. L. Tietze, H. Kleemann, C. Hoßbach, J. W. Bartha, A. Zakhidov, K. Leo, *Nat Commun* **2013**, 4, 2775.

Fast Near-Infrared Photodetection using III-V Colloidal Quantum Dots

